Tissue-Specific Immunosuppressive and Proliferating Macrophages Fuel Early Metastatic Progression of Human Colorectal Cancer to the Liver

Paolo Marzano[1,2], Cristiana Soldani[3], Valentina Cazzetta[2], Barbara Franceschini[3], Sara Terzoli[2], Anna Carletti[2], Michela Anna Polidoro[3], Federica Marchesi[1], Massimo Locati[1,4], Gianluca Basso[5], Ana Lleo[3,6], Guido Costa[6,7], Guido Torzilli[6,7], Flavio Milana[6,7], Rocco Piazza[8], Paola Spaggiari[9], Luca Di Tommaso[6,9], Joanna Mikulak[2], Domenico Mavilio[1,2], and Matteo Donadon[10,11]

ABSTRACT

Early synchronous colorectal liver metastasis (CRLM) represents a clinical condition characterized by the simultaneous presence of primary colorectal cancer and metastatic liver lesions. In this study, we characterized the tissue-specific transcriptomes, phenotypes, and functional relevance of tumor-associated macrophages (TAM) within the tumor microenvironment (TME) of colorectal cancer and CRLM specimens from patients who underwent simultaneous surgical removal of these malignancies. The high-throughput single-cell transcriptional analysis revealed an inverse ratio of inflammatory and immunoregulatory TAMs in the colorectal cancer and CRLM TMEs, along with heterogeneity in both tumoral tissues. Furthermore, we found that inflammatory TAMs in colorectal cancer expressed inhibitory ligands that might support immune escape, thus favoring liver metastatic progression. In contrast, CRLM lesions possessed a highly immunosuppressive milieu characterized by large proliferative *CTLA4*$^+$ immunoregulatory TAMs and the presence of *IL7R*$^+$ cytotoxic TAMs. Higher frequencies of these specific TAM subsets in CRLM were associated with shorter disease-free survival and worse patient prognosis. The identification and characterization of immunoregulatory TAMs preferentially enriched in CRLM is key for the development of novel immunotherapeutic strategies aimed at boosting anticancer immune responses within the TME.

Introduction

Colorectal cancer (CRC) represents one of the most frequent malignancies worldwide, with more than 50% of patients developing colorectal liver metastasis (CRLM; refs. 1, 2). Among them, simultaneous synchronous CRLM represents a particularly challenging clinical entity, occurring in approximately 15% to 25% of colorectal cancer cases (3). This clinical setting reflects an early disease phase, with concurrent primary tumors and liver metastases. The standard treatment combines systemic chemotherapy and surgical resection, but the 5-year survival rate is only 50% with heterogeneous clinical outcomes and responsiveness to treatments (4, 5).

The clinical variability observed in patients may stem not only from tumor-intrinsic changes but also from immune alterations within the tumor microenvironment (TME; refs. 6, 7). In this scenario, tumor-associated macrophages (TAM) can remarkably accelerate tumor progression, invasion, and dissemination through various mechanisms (8, 9). The role of these innate immune effectors is complex as they can exhibit a high degree of plasticity and can be polarized into either inflammatory/antitumorigenic (conventionally referred to as M1-like TAMs) or immunoregulatory/protumorigenic (conventionally referred to as M2-like TAMs) phenotypes depending on the signals they receive within the TME (10). TAM clinical relevance has been reported in many different cancer types (11, 12). Recently, we identified a distinct subtype of TAMs, termed large TAMs, according to their morphology, which is more highly enriched in patients with CRLM with the worst prognosis. In particular, we found that these large TAMs exhibit high cellular complexity with intracellular vacuoles, and their prognostic relevance parallels a peculiar functional diversity in CRLM (13, 14). Nonetheless, we still do not know whether the enrichment of large TAM subsets represents a peculiar phenomenon of the TME of CRLM or whether it is also present in the TME of matched primary tumors. Even the characterization at single-cell level of large TAMs is still lacking, and this is an important knowledge gap considering the significantly higher recurrence rates for patients with CRLM compared with those with primary colorectal cancer (15–17).

In the present study, we performed single-cell RNA sequencing (scRNA-seq) of peritumoral samples from three patients with early synchronous CRLM who underwent simultaneous surgical resection

[1]Department of Medical Biotechnology and Translational Medicine, University of Milan, Milan, Italy. [2]Unit of Clinical and Experimental Immunology, IRCCS Humanitas Research Hospital, Milan, Italy. [3]Laboratory of Hepatobiliary Immunopathology, IRCCS Humanitas Research Hospital, Milan, Italy. [4]Department of Immunology and Inflammation, IRCCS Humanitas Research Hospital, Milan, Italy. [5]Genomic Unit, IRCCS Humanitas Research Hospital, Milan, Italy. [6]Department of Biomedical Sciences, Humanitas University, Milan, Italy. [7]Division of Hepatobiliary and General Surgery, IRCCS Humanitas Research Hospital, Milan, Italy. [8]Department of Medicine and Surgery, University of Milan-Bicocca, Monza, Italy. [9]Department of Pathology, IRCCS Humanitas Research Hospital, Milano, Italy. [10]Department of Health Sciences, Università del Piemonte Orientale, Novara, Italy. [11]Department of General Surgery, University Maggiore Hospital Della Carità, Novara, Italy.

J. Mikulak, D. Mavilio, and M. Donadon contributed equally to this article and share last authorship.

Corresponding Author: Domenico Mavilio, Unit of Clinical and Experimental Immunology, Department of Medical Biotechnology and Translational Medicine, University of Milan School of Medicine, IRCCS Humanitas Research Hospital, Via Alessandro Manzoni, 56 Rozzano, Milan 20089, Italy. E-mail: domenico.mavilio@unimi.it

Cancer Immunol Res 2025;13:1783–97

doi: 10.1158/2326-6066.CIR-25-0031

of primary and metastatic lesions. To provide insights into the mechanisms behind the progression of early-stage diseases, the purpose of this work was to examine the transcriptional heterogeneity and diversity of TAMs within the TME. Our results revealed an inverse ratio of inflammatory and immunoregulatory TAMs in the colon and liver, along with heterogeneity in both tissues. Moreover, we found that colon-associated inflammatory TAMs expressed inhibitory ligands that might support immune escape, thus favoring liver metastasis. Furthermore, and in contrast with the primary tumor, CRLM lesions possessed a highly immunosuppressive milieu characterized by the presence of proliferative and immunoregulatory *CTLA4*$^+$ TAMs and cytotoxic *IL7R*$^+$ TAMs.

Materials and Methods

Study approval and patient information

All patients enrolled in this study ($n = 18$, **Table 1**) were histologically confirmed as having synchronous CRLM and underwent simultaneous surgical resection of the primary colorectal tumor and liver metastases at IRCCS Humanitas Research Hospital. Written informed consent for tissue collection and biobanking was provided. The study was conducted in accordance with the ethical principles outlined in the Declaration of Helsinki (1975) and approved by the IRCCS Humanitas Research Hospital Ethics Committee (protocol number 282/19). Patients were enrolled regardless of *KRAS* mutation status.

Table 1. Demographics and clinical–pathologic data.

Variable	Data
Number of patients	18
Gender	
M/F, *n* (%)	10 (55.5)/8 (45.5)
Age (year), median (range)	64 (39–77)
Size of CRLMs (cm), median (range)	1.8 (0.7–13)
Number of CRLMs, median (range)	2 (1–19)
Bilateral (liver) disease, *n* (%)	7 (38.8)
Preoperative CEA, median (range)	3.8 (0.5–147)
Grading of the primary CRC	
G1–2, *n* (%)	15 (83.4)
G3–4, *n* (%)	3 (16.6)
Staging of the primary CRC	
T status, T3–4, *n* (%)	12 (66.6)
N status, N+, *n* (%)	9 (50)
Synchronous presentation, *n* (%)	18 (100)
Site of primary CRC	
Right colon, *n* (%)	8 (44.4)
Left colon	4 (22.2)
Rectum, *n* (%)	6 (33.4)
Neoadjuvant chemotherapy, *n* (%)	12 (66.6)
Chemotherapy lines, median (range)	1 (1,2)
Type of chemotherapy, *n* (%)	
Oxaliplatin-based	9 (50)
Irinotecan-based	9 (50)
+Anti-VEGF	12 (66.6)
+Anti-EGFR	6 (33.4)
RAS mutated, *n* (%)	7 (38.8)
Simultaneous resection, *n* (%)	18 (100)
Type of analysis	
IHC	18 (100)
scRNA-seq	3 (16.6)

Abbreviations: CEA, carcinoembryonic antigen; CRC, colorectal cancer; G, grade; N, node; T, tumor.

Fresh peritumoral tissue samples from both the colon and liver were collected intraoperatively in 5 mL of RPMI 1640 media (Euroclone, cat # ECB9006L; lot EUM023P), specifically from areas adjacent to the tumor core and devoid of visible necrosis or hemorrhage. Peripheral blood was collected from the same patients.

scRNA-seq was performed on matched tumor (colon and liver) and blood samples from three patients (CRLM-1, CRLM-2, CRLM-3; $n = 3$, **Table 1**). For validation, IHC was carried out on a retrospective cohort of 18 patients with early synchronous CRLM who underwent simultaneous surgical resection of primary and metastatic lesions between January 2020 and December 2024 at IRCCS Humanitas Research Hospital, namely the three patients profiled by scRNA-seq and 15 additional cases selected using identical clinical and pathologic criteria (**Table 1**).

Isolation of cells and sorting

Peritumoral colon and liver tissue samples, surgically sampled from tissue area adjacent to the tumor mass, were chopped into small fragments, digested in Hank's Balanced Salt Solution+/+ (Euroclone, cat # ECM0507L; lot EUM026R) containing 2 mg/mL of collagenase type I solution (Gibco, cat # 17100-017; lot 2802331), 2% FBS (Sigma-Aldrich, cat # F7524-500ML; lot BCCD0778), 50 μg/mL DNAse I (Sigma-Aldrich), and 10 mmol/L HEPES (Sigma-Aldrich, cat # H0887-100ML; lot RNBM3396), and subsequently incubated for 35 minutes at 37°C in the same solution. The resulting single-cell suspensions were filtered through a 100-μm cell strainer, and erythrocytes were lysed with BD Lysing Buffer (cat # 555899; lot 4068991). Cells were pelleted, counted, and subsequently cryopreserved in cryovials containing 1 mL of FBS (Sigma-Aldrich, cat # F7524-500ML; lot BCCD0778) supplemented with 10% DMSO (PanReac AppliChem), as previously published (18). Samples were initially stored at −80°C and subsequently transferred to liquid nitrogen for long-term preservation until further processing. Next, the cells were thawed, washed in PBS, stained with Live/dead Aqua Fluorescent Reactive Dye (Thermo Fisher Scientific, cat # L34967; lot 2775959) and the mouse anti-human CD45 2D1 (BD Biosciences, cat # 560178, RRID: AB_1645479; lot 1306196) at 4°C for 20 minutes, and sorted using a FACS Melody cell sorter (BD Biosciences, RRID: SCR_023209).

From the same patients, fresh peripheral blood mononuclear cells (PBMC) were isolated through Lympholyte-H Cell Separation density gradient solution (Cedarlane Laboratories) according to the manufacturer's instructions and frozen in FBS (Sigma-Aldrich, cat # F7524-500ML; lot BCCD0778) supplemented with 10% of the cryoprotective DMSO (PanReac AppliChem; ref. 18).

IHC

Consecutive tissue sections 2-μm thick were prepared from formalin-fixed and paraffin-embedded tissues provided by the Pathology Department of the Humanitas Clinical and Research Center and processed for IHC. Briefly, after deparaffinization and rehydration, antigen retrieval was performed by heat treatment using Diva Decloaker solution 100× (Bio-Optica, cat # BRI2006 L; lot 061223A) in a pressure cooker at 120°C for 5 minutes. Endogenous peroxidases were blocked by incubation with Peroxidase-Blocking Solution (Agilent, cat # s2023; lot 20076272) for 15 minutes at room temperature. The sections were then incubated with the primary rabbit anti-human proliferating cell nuclear antigen (PCNA) D3H8P (Cell Signaling Technology, cat # 13110, RRID: AB_2636979; lot 7, monoclonal, 1:100) for 2 hours at room temperature, followed by incubation with the Dako EnVision+ System- HRP Labeled Polymer Anti-Rabbit

(Agilent, cat # K4003, RRID: AB_2630375; lot 11523704). Diaminobenzidine tetrahydrochloride (Biocare Medical, DAB Chromogen Kit DB801; lot 101823A-4) was used as a chromogen (brown). Double staining was performed with incubation of the anti-human CD163 10D6 (Leica Biosystems, cat # NCL-L-CD163, RRID: AB_2756375; lot 6098050; 1:200) for 2 hours at room temperature on the same tissue sections previously marked with anti-PCNA, followed by incubation with the Dako EnVision+ System- HRP Labeled Polymer Anti-Mouse (Agilent, cat # K4001, RRID: AB_2827819; lot 11292400). An AEC staining kit (Sigma-Aldrich, cat # AEC101-1KT, lot 0000210570) was used as a chromogen (red). Nuclei were lightly counterstained with a freshly made hematoxylin solution (Histo-Line Laboratories, cat # 01HEMM1000; lot HEMM-35/21). For single IHC CD45 antibody clone PD7/26 + 2B11 (Agilent, cat #M0701, RRID: AB_2314143; lot 41827598) 1:200 or CD163 antibody 10D6 (Leica Biosystems, cat # NCL-L-CD163, RRID: AB_2756375; lot 6098050) 1:200 were used, followed by incubation with the Dako EnVision+ System- HRP Labeled Polymer Anti-Mouse (Agilent, cat# K4003, RRID: AB_2630375; lot 11523704). Images were captured by light microscopy using an Olympus BX51 microscope with 10× and/or 40× magnification. The images were processed by Photoshop.

Single-cell RNA library preparation

Libraries for scRNA-seq (three patients, eight matched libraries—three colon $CD45^+$, three liver $CD45^+$, and two PBMCs) were generated using a microfluidic-based approach on the Chromium Single-Cell Platform using the Chromium Single-Cell 5′ Library and Gel Bead Kit (10× Genomics, 1000006) according to the manufacturer's instructions. In brief, thawed samples were evaluated for viability prior to scRNA-seq analysis, and all were ≥95% viable. Single cells were individually loaded onto a Chromium single-cell controller (10× Genomics) to generate single-cell gel beads-in-emulsion. Captured cells were then lysed, and the released RNA was barcoded through reverse transcription in individual gel beads-in-emulsion. The concentration of the scRNA-seq libraries was assessed using an Agilent 4200 TapeStation system. The libraries were sequenced using an Illumina NovaSeq 6000 sequencer with a paired-end 150-bp (PE150) reading strategy (performed by CapitalBio Technology).

Processing scRNA-seq data

Fastq files were processed with Cell Ranger v7.1.0 (10× Genomics, RRID: SCR_023221) using default parameters. The scRNA-seq reads were aligned to the GRCh38 (version refdata-gex-GRCh38-2020-A, 10× Genomics) human genome reference. Only mapped reads with valid barcodes and unique molecular identifiers (UMI) were retained to compute a gene expression matrix containing the number of UMI for every cell and gene. Gene counts were then imported into Python (v3.9.7, RRID: SCR_008394) and processed with Scanpy (v1.9.3, RRID: SCR_018139; ref. 19). Each sample was QC-filtered independently. Cells with fewer than 500 and more than 4,000 expressed genes, or fewer than 950 and more than than 12,000 UMIs; greater than 10% of mitochondrial genes; and less than 0.05% of ribosomal genes were removed. Doublets were computationally identified and removed using Single-Cell Remover of Doublets (v0.2.3, RRID: SCR_018098; ref. 20). Raw data matrices of all samples ($n = 8$) were then merged in one single AnnData object (v0.10.4, RRID: SCR_018209; ref. 21) and were then log-normalized with a scale factor of 10,000. Highly variable genes (HVG, $n = 4{,}000$) were identified across each sample (*batch_key = "sample_identity"*) using the *Seurat_v3* dispersion-based methods on raw counts, and data from each sample were integrated and batch-corrected with the single-cell Variational Inference (scVI)-tools algorithm (v1.0.0; ref. 22). In brief, the setup of the model was performed with the *scvi.model.SCVI.setup_anndata()* function, setting as *batch_key* the *patient_ID* covariate, and with the *scvi.model.SCVI()* function, setting *n_layers = 2*, *n_latent = 30*, and *gene_likelihood = "nb"* parameters. The clustering analysis was performed using the Leiden algorithm (23), and the clusters were then embedded in two-dimensional Uniform Manifold Approximation and Projection (24) using the scVI batch-corrected latent space. For the reclustering of cells of interest, we extracted cells from the total dataset, recomputed the HVGs on raw counts, and retrained the scVI model with the same settings reported above.

Analysis of publicly available healthy liver and healthy blood scRNA-seq databases

The scRNA-seq raw counts of healthy liver samples ($n = 5$) and healthy blood samples ($n = 6$, at baseline) were downloaded from Gene Expression Omnibus (GEO) datasets accession numbers GSE136103 (RRID: SCR_005012; ref. 25) and GSE260763 (26, 27), respectively, and then imported into Python (v3.9.7) and processed with Scanpy (v1.9.3) with the same workflow reported above.

Differentially expressed gene analysis

Differentially expressed genes (DEG) were computed using the *FindAllMarkers()* function to identify the cluster-specific and cell cycle–specific genes, and *FindMarkers()* function to identify the inflammatory- and immunoregulatory-specific genes between the colon and liver, implemented in Seurat (v4.4.0, RRID: SCR_007322; ref. 28) under R v4.3.2. Briefly, the AnnData object was converted to a Seurat object (.h5Seurat) with the *Convert()* function implemented in SeuratDisk (v0.0.0.9020), setting *dest = h5seurat* and *assay = RNA* parameters, and read with the *LoadH5Seurat()* function. DEGs were computed on raw counts setting *test.use = negbinom*, *logfc.threshold = 0*, and *min.pct = 0.1* parameters, setting adjusted P value < *0.05* and */$\log_2$ fold change/ > 0.25* as cutoff for significance.

Gene module scores and cell-cycle scores

Gene module scores were calculated with specific gene lists, reported as Supplementary tables or specified in the Figure legends, with the Scanpy-implemented *scanpy.tl.score_genes()* function.

To compute the large and small TAM scores, we used the list of DEGs from the published bulk RNA-seq comparison of small and large TAMs (13). Briefly, we filtered the genes for FDR < 0.05; we considered genes with a *$\log_2$ fold change* > 2.5 for large TAMs and genes with a *$\log_2$ fold change* < −2.5 for small TAMs. We then calculated two independent principal component analyses (29) on the two lists with the Scanpy-implemented *scanpy.tl.pca()* function, setting *svd_solver = "arpack"* and *use_highly_variable = False*, on the liver macrophages clusters (L0–8). We extracted the top 20 highest genes characterizing the principal component 1 (PC1), ranked according to their loading values. We then used the *scanpy.tl.score_genes()* function to compute the two scores.

To evaluate the cell-cycle phase, we first calculated for each cell a score based on the expression of S and G2M phase markers with the Scanpy-implemented *scanpy.tl.score_genes_cell_cycle()* function, and cells expressing neither of them have been associated with the G1 phase (30).

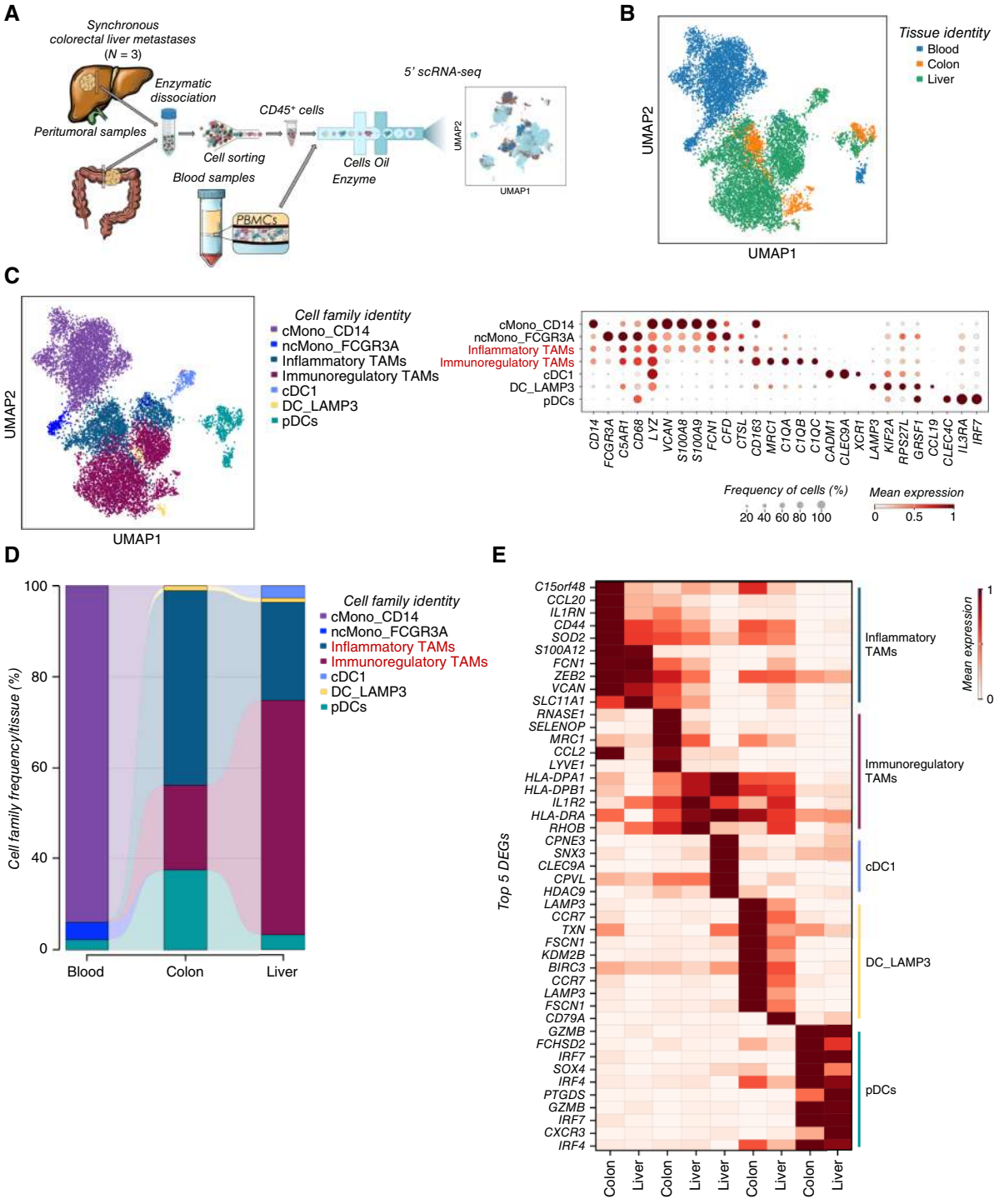

Figure 1.

Myeloid cell characterization in synchronous metastatic colorectal cancer by scRNA-seq. **A,** Schematic overview of the experimental workflow depicting sample processing and scRNA-seq of matched peritumoral samples of primary colorectal cancer ($n = 3$), metastatic liver tumor ($n = 3$), and peripheral blood cells ($n = 2$). **B,** Tissue-integrated UMAP of the myeloid cell reclustering, a total of 11,283 single cells from all the patients (CRLM-1–3, $n = 3$), color-coded by tissue assignment. **C,** UMAP plot (left) color-coded by the main myeloid cell families. The dot plot (right) shows the expression of canonical markers used for the annotation of the cell families, in which the dot size indicates the proportion of expressing cells and the color indicates the normalized mean expression levels. **D,** Fractions (%) of cell families detected in each tissue, colored as in (**C**), normalized on the total cells per tissue. The alluvial plot shows the correspondence between cell families and tissues, in which the stratum indicates the contribution of each cell family in each tissue as frequency and the flow indicates the shared cell families among tissues. **E,** The heatmap shows the scaled gene expression of the top five DEGs identified among the colon and liver cell families reported on the right.

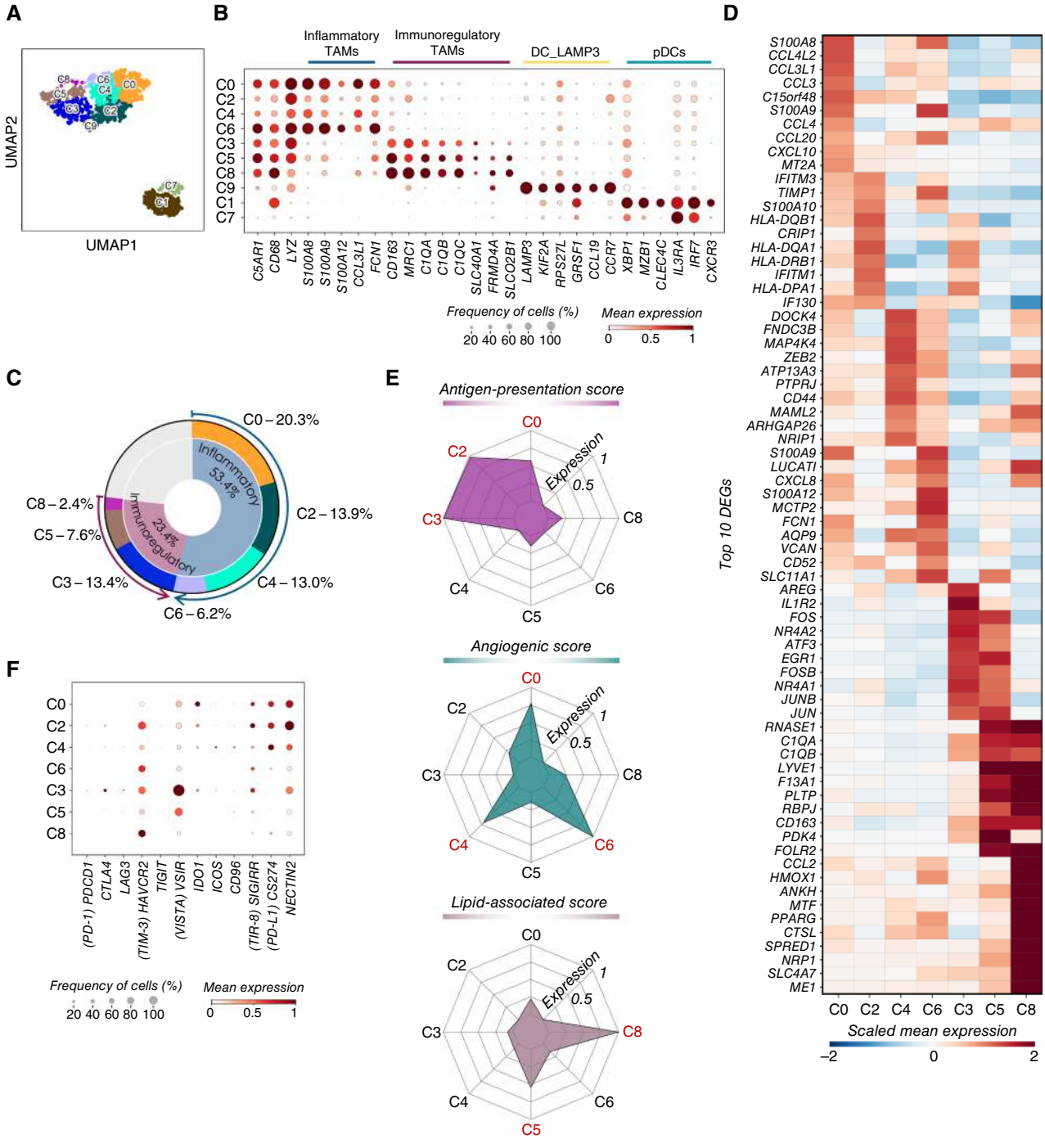

Figure 2.

Heterogeneity of TAM transcriptional profiles in the colon peritumoral area. **A,** UMAP clustering projection of the integrated colon myeloid immune cells from all the patients (*n* cells = 1,127). **B,** The dot plot shows the expression of canonical markers used for the annotation of myeloid cell subtypes, in which the dot size indicates the proportion of expressing cells, colored by normalized mean expression levels, and the clusters are reordered according to cell family. **C,** The nested pie chart shows the percentage frequency distribution of each cluster (outer circle) and the cell family correspondences (inner circle), colored as in **Fig. 1C**. DC clusters are reported in gray. **D,** The heatmap shows the scaled gene expression of the top 10 DEGs (rows) per cluster (columns) identified among the colon macrophage clusters (C0, C2–6, and C8). DC clusters (C1, C7, and C9) were excluded from the analysis. **E,** The radar plots show the mean expression levels of the antigen-presentation (*n* genes = 24), lipid-associated (*n* genes = 32), and angiogenic (*n* genes = 31) scores per cluster. Clusters with the highest scores for each signature are highlighted in red. **F,** The dot plot shows the expression of immune checkpoint and ligand genes, in which the dot size indicates the proportion of expressing cells, colored by normalized mean expression levels, and the clusters are reordered according to cell family. DC clusters (C1, C7, and C9) were excluded from the analysis.

Pseudotime analysis

Pseudotime trajectory analysis was performed by Monocle2 (v2.8.0, RRID: SCR_016339; ref. 31) under R v4.3.2 on normalized gene expression counts. HVGs (n = 4,000) were recomputed in Scanpy only considering TAM clusters and were imported in R and set as the trajectory ordering genes. These were identified in a tissue-

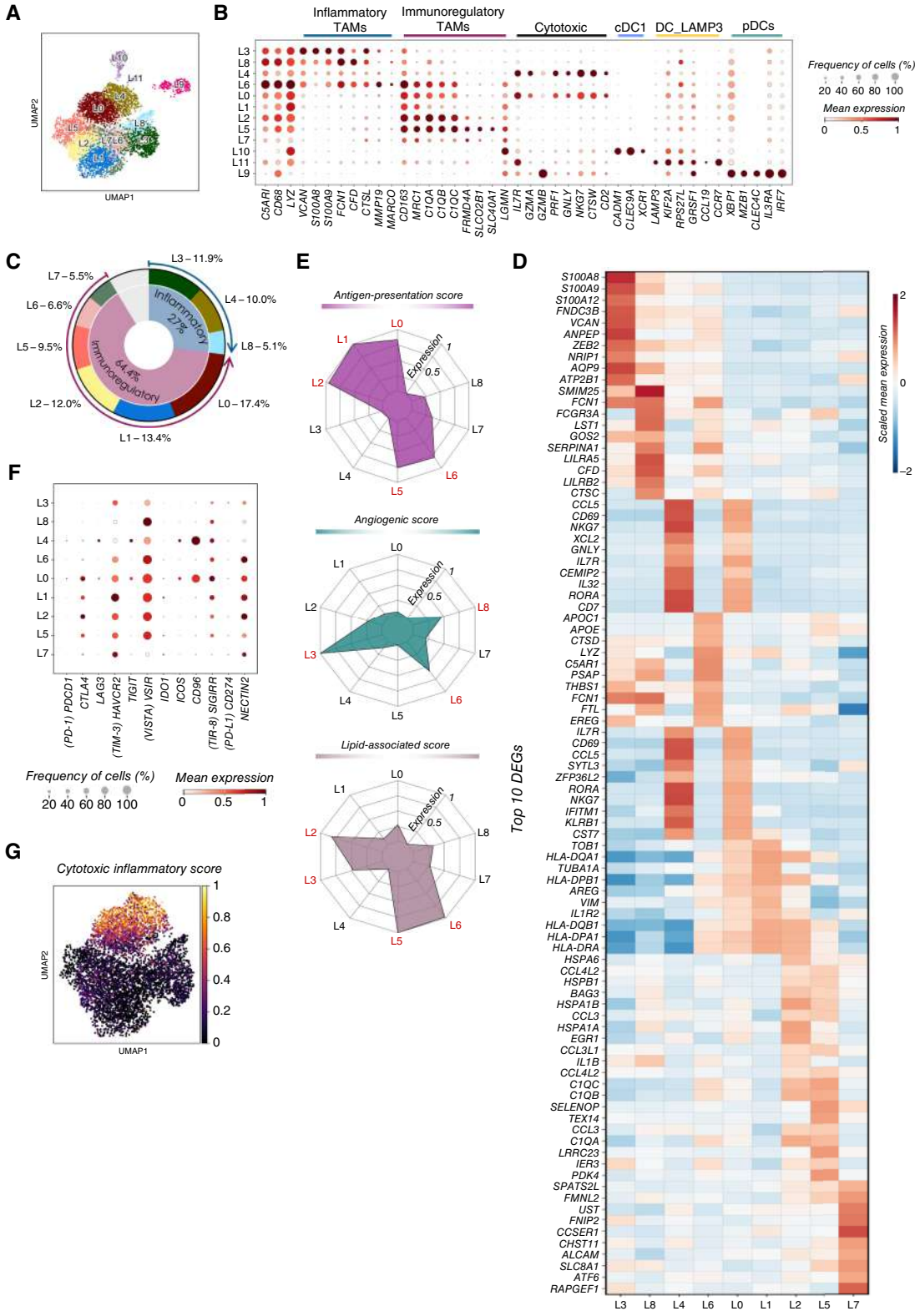

based manner (*batch_key = "tissue_identity"*) and subsequently filtered to retain only the 4,000 most variable across tissues to avoid redundancy. A single-cell trajectory was constructed by the Discriminative Dimensionality Reduction with Trees (DDTree) algorithm on all the cells belonging to the blood, colon, and liver, except for dendritic cells (DC). No starting root was set as starting point of the trajectory. The trajectory visualization was conducted by the *plot_cell_trajectory()* function implemented in Monocle2.

Reactome pathway analysis

Pathway enrichment pathway analysis was performed using the Reactome web tool (https://reactome.org/, RRID: SCR_003485). The Reactome pathways of cell type were enriched using DEGs with adjusted P value < 0.05 and $\log_2$ fold change > 0.25. Only pathways with FDR < 0.05 and composed of at least three genes were selected as significant and visualized by the ggplot2 package under R v4.3.2 as circular bar plots, in which the bar length corresponds to the $-\log_{10}$ of the P value of the pathways.

Statistics

Continuous variables were presented as a range with a median, and discrete variables were presented as a number and percentage. Variables were analyzed using the χ^2 test or the Mann–Whitney U test where appropriate. Survival analyses were performed using the Kaplan–Meier curves to analyze differences in disease-free survival and compared using the log-rank Mantel–Cox test. Survival was calculated from the day of surgery. The effect size was reported as HR and 95% confidence interval, P values, and survival plots. Statistical computations were conducted using the software Stata (v16, RRID: SCR_012763) and GraphPad PRISM (v10.2.3, RRID: SCR_002798). A P value less than 0.05 was considered significant for all tests and was represented with GraphPad style and summarized with the following number of asterisks (*): *, $P < 0.05$; ***, $P < 0.001$; and ****, $P < 0.0001$.

Results

Single-cell transcriptomic profile of macrophages in early phases of synchronous CRLM

To investigate heterogeneity within the TAM populations and depict differences between primary colon tumor and liver metastasis, we isolated CD45$^+$ leukocytes from the peritumoral area of matched colon and liver tumor samples and from PBMCs (Supplementary Fig. S1A and S1B) of three patients (CRLM-1–3) who underwent simultaneous synchronous colorectal–liver resections on the same day. We then performed high-throughput scRNA-seq analysis on these human specimens (**Fig. 1A**; Supplementary Fig. S1C).

Through gene profiling, the main populations of myeloid cells within tumor-associated leukocytes and PBMCs were identified: these included blood monocytes (Mono) and tissue macrophages (TAMs) expressing *CD14*, CD16 (*FCGR3A*), CD88 (*C5AR1*), *CD68*, *LYZ*, and *VCAN,* and DCs, expressing *CD1C*, *CLEC9A*, *CLEC10A*, *IL3RA*, and *CLEC4C* (Supplementary Fig. S1D and S1E). Despite previous studies documenting transcriptome profiles of macrophages (32), detailed transcriptome annotations that can comprehensively capture the dynamic changes of macrophages from the primary to the metastatic site are not available or being published. Hence, to identify distinct transcriptional programs of macrophages simultaneously populating the colon and corresponding liver metastases, we further subclustered the myeloid-enriched clusters by refining a total of 11,283 cells, which were spatially represented through Uniform Manifold Approximation and Projection (UMAP; **Fig. 1B**). Based on the expression of known markers expressed by the main myeloid populations in tissues and peripheral blood, we identified (i) the classic monocytes (cMono_CD14) and nonclassic monocytes (ncMono_FCGR3A) according to the expression of *CD14* or *FCGR3A* genes, respectively, and (ii) macrophages, expressing *CD68*, *LYZ*, and *C5AR1*, which we further annotated into inflammatory (*VCAN*, *S100A8*, *S100A9*, *FCN1*, *CFD*, and *CTSL*) and immunoregulatory (*CD163*, *MRC1*, and *C1QA–C*) TAMs (33, 34). Furthermore, we identified three main subsets of DCs according to their lineage signatures: (i) type 1 conventional DCs (cDC1; *CADM1*, *CLEC9A*, and *XCR1*); (ii) DC_LAMP3 (*LAMP3*, *KIF2A*, *RPS27L*, *GRSF1*, and *CCL19*); and (iii) plasmacytoid DCs (pDC; *CLEC4C*, *IL3RA*, and *IRF7*; **Fig. 1C**; ref. 35). By comparing the frequencies of the TAM clusters between colon and liver, we found an inversed inflammatory/immunoregulatory ratio within the two tissues. Indeed, in the colon, the main population was inflammatory TAMs (53.4%), relative to 27% in the liver, whereas the liver was enriched in immunoregulatory TAMs (64.4%), relative to the colon (23.4%; **Fig. 1D**). Moreover, these two TAM families were characterized by unique and different transcriptomic profiles within the two tissues (**Fig. 1E**).

Colon-associated inflammatory TAMs are involved in tumor immune evasion

To better characterize inflammatory and immunoregulatory TAM populations in the colon, we independently analyzed myeloid cells. Following high-resolution clustering, the colon myeloid cells clustered into 10 distinct populations (**Fig. 2A**). By supervised annotation (**Fig. 2B**), clusters *S100A8*_C0, *IFITM3*_C2, *DOCK4*_C4, and *S100A9*_C6 were found to be enriched in inflammatory TAMs, whereas clusters *AREG*_C3, *RNASE1*_C5, and *CCL2*_C8 were enriched in immunoregulatory TAMs. Regarding DCs, the *LAMP3*_C9 cluster was identified as DC_LAMP3, whereas *GZMB*_C1 and *SEL1L3*_C7 clusters were identified as pDCs. This annotation further confirmed the above-reported abundance of inflammatory TAMs in the colon (53.4%; **Figs. 1D** and **2C**). Nonetheless, even though clusters belonging to the same inflammatory or immunoregulatory family share a common backbone-gene

Figure 3.

Heterogeneity of TAM transcriptional profiles in the liver peritumoral area. **A,** UMAP clustering projection of the integrated liver myeloid immune cells from all the patients (n cells = 6,127). **B,** The dot plot shows the expression of canonical markers used for the annotation of myeloid cell subtypes, in which the dot size indicates the proportion of expressing cells, colored by normalized mean expression levels, and the clusters are reordered according to cell family. **C,** The nested pie chart shows the percentage frequency distribution of each cluster (outer circle) and the cell family correspondences (inner circle), colored as in **Fig. 1C**. DC clusters are reported in gray. **D,** The heatmap shows the scaled gene expression of the top 10 DEGs (rows) per cluster (columns) identified among the liver macrophage clusters (L0–8). DC clusters (L9–11) were excluded from the analysis. **E,** The radar plots show the mean expression levels of the antigen-presentation (n genes = 24), lipid-associated (n genes = 32), and angiogenic (n genes = 31) scores per cluster. Clusters with the highest scores for each signature are highlighted in red. **F,** The dot plot shows the expression of immune checkpoint and ligand genes, in which the dot size indicates the proportion of expressing cells, colored by normalized mean expression levels, and the clusters are reordered according to cell family. DC clusters (L9–11) were excluded from the analysis. **G,** The feature plot shows the expression of the cytotoxic inflammatory score (n genes = 21). DC clusters (L9–11) were excluded from the UMAP plot.

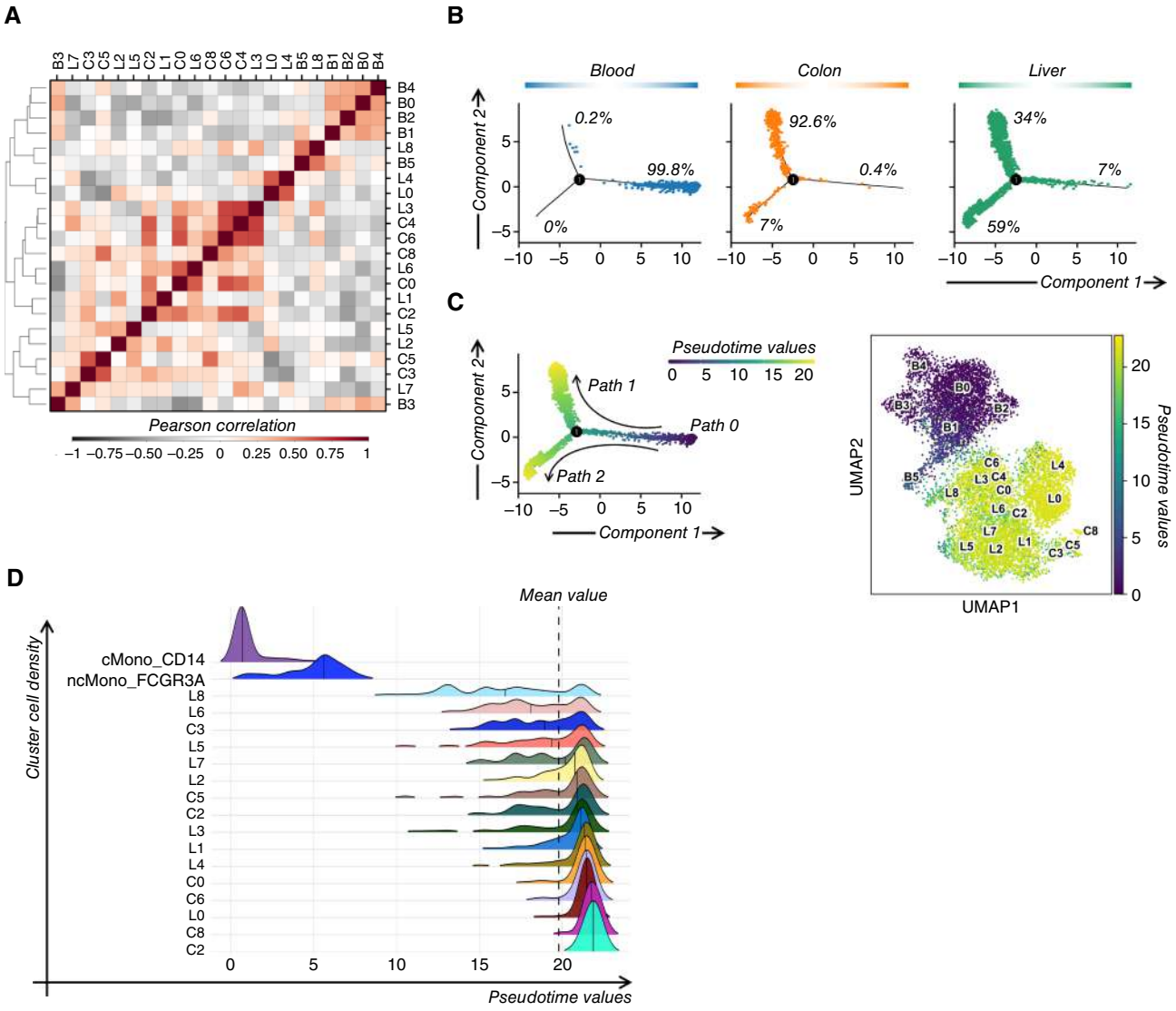

Figure 4.

Transcriptomic correlation and trajectory analysis reveal both similarities and tissue-specific traits in colon and liver TAMs. **A,** The correlation matrix shows the unsupervised hierarchical clustering computed using the Pearson correlation coefficient taking into consideration all the monocytes (blood) and macrophages (colon and liver) clusters. DC clusters were excluded from the analysis. **B,** The ordering of different cell clusters along pseudotime in a two-dimensional state-space defined by Monocle2. The pseudotime trajectory was computed on all the monocytes (blood) and macrophages (colon and liver) clusters, without including DC clusters and setting the starting root. Each point corresponds to a single cell, color-coded according to the tissue identity with the proportions of cells per branch. **C,** Left, the pseudotime trajectory is color-coded according to the pseudotime value, in which each dot corresponds to a single cell. Right, the Monocle2 pseudo-temporal ordering of cells is superimposed on the UMAP plot, in which cells are colored based on their progression along the pseudo-temporal space. **D,** Cell density distribution plot representing cluster frequency (*y*-axis) along the pseudotime (*x*-axis). The median pseudotime value of each distribution is indicated by the solid line, whereas the total mean pseudotime value is indicated by the dotted line.

signature, we identified high heterogeneity in the transcriptomes of inflammatory and immunoregulatory TAMs (**Fig. 2D**; Supplementary Table S1). Indeed, inflammatory TAMs were characterized by the upregulation of specific genes associated with responsiveness to chemotactic signals and migration to inflammation sites. This latter transcriptomic profile includes the S100 gene family (*S100A8*, *S100A9*, and *S100A12*) and several proinflammatory genes (i.e., *CCL3*, *CCL3L1*, *CCL4*, *CCL4L2*, *CXCL8*, and *CXCL10*) known to prime the initiation of inflammatory signal transduction and the production of proinflammatory cytokines (36). Furthermore, the elevated expression of *VCAN* in cluster *S100A9*_C6 indicates a role in extracellular matrix regulation and tissue remodeling, thus suggesting a potential proregenerative function within this macrophage subset (37). Cluster *IFITM3*_C2 was further characterized by high expression of antigen-presenting genes such as *HLA-DQB1*, *HLA-DQA1*, *HLA-DRB1*, and *HLA-DPA1*. In contrast, macrophages expressing *CD163* are typically categorized as immunoregulatory TAMs and exhibit properties favorable for anti-inflammatory

functions and tissue remodeling (38). These features were evident in the colon within clusters *AREG*_C3, *RNASE1*_C5, and *CCL2*_C8. The high expression of the C1q gene family (*C1QA*, *C1QB*, and *C1QC*), along with high levels of *CD163*, *CCL2*, *HMOX1*, and *PPARG* genes, indicates an active role in recruiting immune cells to sites of inflammation and suggests a polarization toward an anti-inflammatory phenotype. Additionally, the presence of molecules such as *AREG*, *IL1R*, *FOS*, and *JUN* within these latter myeloid clusters are crucial in fine tuning immune responses, modulating inflammation, and supporting tissue health and repair.

By analyzing multiple genes at once and computing distinct gene scores instead of focusing on the expression of individual genes, we were able to further characterize each cluster based on its functional characteristics (**Fig. 2E**; Supplementary Table S2; ref. 39). In particular, we identified the following: (i) clusters with antigen-presentation properties (i.e., *S100A8*_C0, *IFITM3*_C2, and *AREG*_C3) suggesting an ability to prime adaptive immune responses; (ii) clusters with lipid-association properties (i.e., *RNASE1*_C5 and *CCL2*_C8) whose enhanced lipid accumulation and metabolism pathways are suggestive of extensive phagocytosis; and (iii) clusters with angiogenic properties (i.e., *S100A8*_C0, *DOCK4*_C4, and *S100A9*_C6), which may contribute to the regulation and support of tissue remodeling. To our surprise, inflammatory TAMs rather than immunoregulatory TAMs expressed higher levels of the ligands of immune checkpoints, including the PD-1 ligand PD-L1 (*CD274*) and the TIGIT ligand *NECTIN2* (**Fig. 2F**). The expression of inhibitory checkpoint ligands on inflammatory TAMs has been already reported to be possibly associated with an immune-escape mechanism to evade T-cell immune surveillance (40). Hence, our results showing high frequencies of inflammatory TAMs expressing inhibitory checkpoint ligands in the TME of colon cancer can explain, at least in part, the lack of immune control of the primary tumor that naturally progresses toward liver metastasis development.

The synchronous CRLM disease alters the physiologic transcriptomic profiles of liver macrophages

In the TME of CRLM, the myeloid cells clustered into 12 distinct populations (**Fig. 3A**). The resident macrophage population in the liver is known as Kupffer cells (KC) and they are transcriptionally defined by strong expression of the *VSIG4* and *CD5L* genes, among others (34). The cluster with the profile closest to KCs (*CCL4L2*_L5) showed very low expression of *CD5L* and other KC genes (Supplementary Fig. S2A). In order to determine whether or not this finding was associated with the CRLM pathologic clinical setting, we compared the profile of this population with KC populating healthy human livers (see "Materials and Methods" section, Supplementary Fig. S2B and S2C; ref. 25). In this different and para-physiologic condition, we clearly annotated KCs, whose signature was highly enriched in cluster HL2 (Supplementary Fig. S2D). The comparison of the *CCL4L2*_L5 cluster profile to HL2 highlighted a down-regulation of several KC-associated genes (i.e., *CD5L*, *VSIG4*, *MS4A4A*, *FOLR2*, *SLC40A1*, *VCAM1*, and others), suggesting that the transcriptomic profiles of KCs were markedly modified in the hepatic TME during the early phases of liver metastasis from colon cancer. Indeed, the lack of a comparable tissue cluster in our pathologic clinical setting suggests a disruption in the typical KC gene expression patterns inside the tumor milieu.

Similar to our analysis of the primary tumor, we analyzed the transcriptomes of myeloid cells within CRLM tissues to determine the immunoregulatory or inflammatory nature of TAMs in the liver metastatic lesions. Clusters *S100A8*_L3, *SMIM25*_L8, and *CCL5*_L4 were annotated as inflammatory TAMs, whereas clusters *IL7R*_L0, *TOB1*_L1, *HSPA6*_L2, *CCL4L2*_L5, and *SPATS2L*_L7 were annotated as immunoregulatory TAMs. *APOC1*_L6 was annotated as a cluster with mixed transcriptional features of inflammatory and immunoregulatory TAMs (**Fig. 3B**), which indeed spatially localized in the *UMAP* plot between the two TAM families. Our annotation confirmed the abundance of immunoregulatory TAMs (64.4%), as above-reported (**Figs. 1D** and **3C**; Supplementary Fig. S2E). *PTGDS*_L9, *CPNE3*_L10, and *LAMP3*_11 clusters were annotated as DCs. As in the colon, we identified heterogeneous populations characterized by different transcriptomic profiles (**Fig. 3D**; Supplementary Table S1). In particular, *S100A8*_L3 and *SMIM25*_L8 clusters distinctly exhibited hallmarks of inflammatory profiles characterized by the upregulation of *S100A8*, *S100A9*, *VCAN*, and *IL1R* genes. Conversely, $CD163^{+}$ immunoregulatory macrophages exhibited peculiar features with high levels of HLA and C1q genes. The dual transcriptional profile identified in cluster *APOC1*_L6 constitutes a unique molecular liver signature, suggesting, within liver metastases, the presence of a specific macrophage subset able to polarize into a proinflammatory or immune-suppressive phenotype upon specific stimuli and therefore to control immune responses or contribute to inflammation and tissue repair. Additionally, we identified *IL7R*_L0, *TOB1*_L1, *HSPA6*_L2, *CCL4L2*_L5, and *APOC1*_L6 as highly characterized by antigen-presentation properties, whereas *S100A8*_L3, *APOC1*_L6, and *SMIM25*_L8 expressed angiogenic properties. Finally, *HSPA6*_L2, *S100A8*_L3, *CCL4L2*_L5, and *APOC1*_L6 showed high lipid-associated scores indicative of phagocytic properties (**Fig. 3E**; Supplementary Table S2). The inhibitory checkpoints CTLA-4 (*CTLA4*) and TIM-3 (*HAVCR2*), whose expression is mainly recognized on T cells, were also expressed by all immunoregulatory TAM clusters (**Fig. 3F**). In this context, other recent studies have reported their expression and function on other immune cells, including macrophages (41, 42).

*IL7R*_L0 and *CCL5*_L4 represent unique tissue clusters specific of the pathologic CRLM and absent in the healthy liver and pathologic colon, and their cytotoxic features were further confirmed by the cytotoxic inflammatory score (**Fig. 3G**; Supplementary Fig. S2F; Supplementary Table S2). They expressed high levels of the IL-7 receptor (*IL7R*) gene, which encodes for the CD127 protein, together with several other genes linked to an NK cell–like cytotoxic activity (i.e., *KLRB1*, *NKG7*, *GNLY*, *GZMA*, and *CTSW*; **Fig. 3B–D**). A similar signature indicative of cytotoxic monocytes (i.e., $IL7R^{pos}$ monocytes) has been already reported both in physiologic and pathologic conditions (i.e., tumor and viral infections; ref. 43). We observed that the transcriptomic signature of *IL7R*_L0 was preferentially associated with an immunoregulatory phenotype, whereas *CCL5*_L4 was linked to an inflammatory phenotype. Moreover, both clusters specifically expressed immunologic checkpoints, including LAG3 (*LAG3*), *TIGIT*, *CD96*, and *ICOS* (**Fig. 3F**), consistent with inhibitory mechanisms already reported for lymphocytes (44–46).

Integration of transcriptomic profiles reveals tissue-specific monocyte–macrophage dynamics

We then proceeded to characterize human circulating monocytes in the peripheral blood of the same patients to get insight into the blood-derivative TAMs in pathologic colon cancers and CRLM (Supplementary Fig. S3A). Our findings revealed the presence of distinct monocyte populations, with the main population

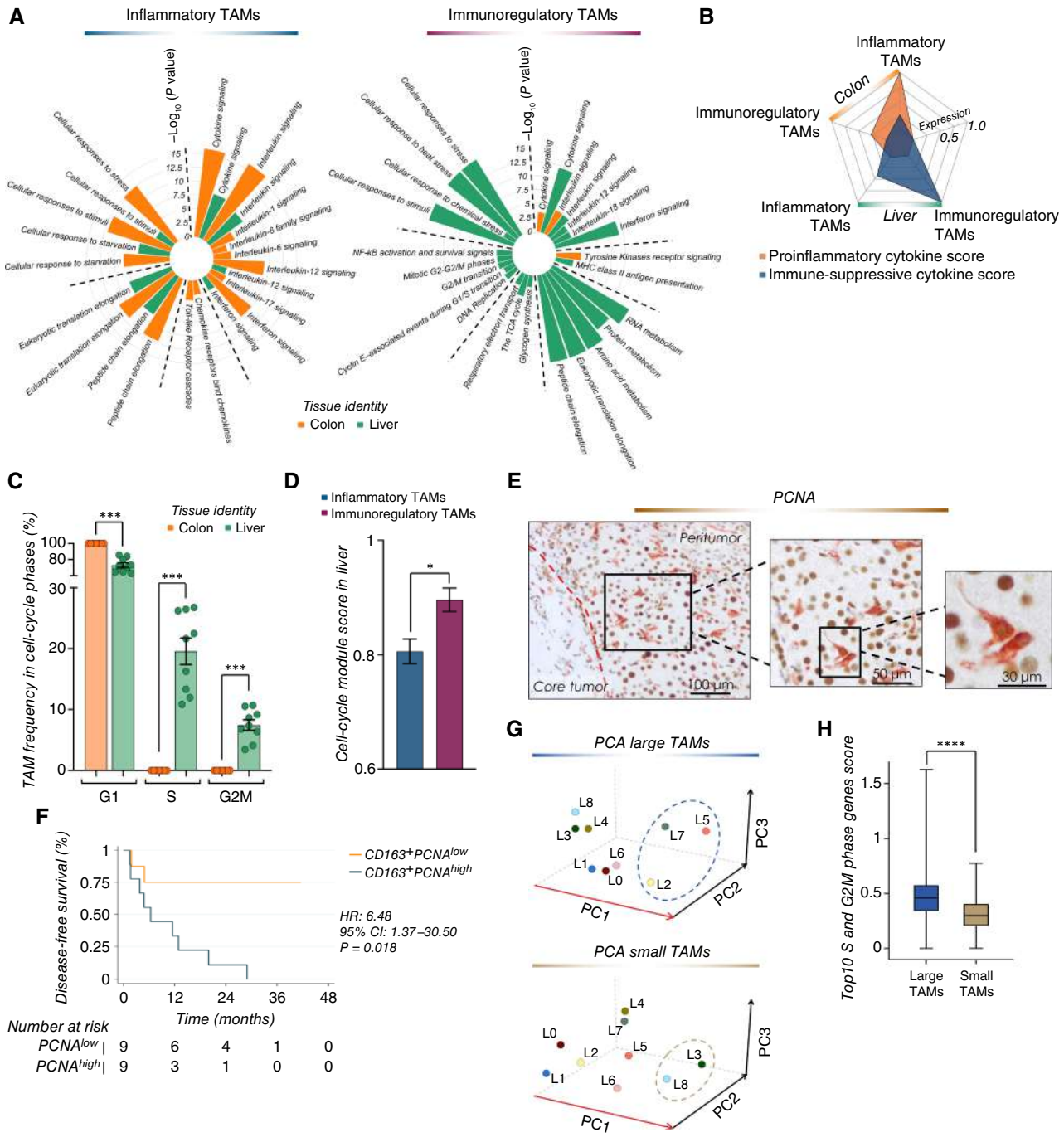

Figure 5.

Transcriptional profile showing proliferative features of liver immunoregulatory TAMs with large macrophages. **A,** The circular bar plots show a selection of significantly enriched pathways with FDR values < 0.05, identified among significant DEGs (percent >10% and adjusted *P* value <0.05 and $\log_2$ fold change >0.25) of inflammatory (left) and immunoregulatory TAMs (right) as the comparison between the colon (orange) and liver (green) using the Reactome pathway browser. The bars are color-coded according to the tissue identity and sized by the $-\log_{10}$(*P* value) value of the pathway enrichment. The dotted lines separate the different pathway groups. **B,** The radar plot shows the mean expression levels of proinflammatory (*TNF*, *IL1A*, *IL1B*, *IL6*, *IL23A*, *CXCL9*, *CXCL10*, and *CXCL11*) and immune-suppressive (*IL10*, *TGFB1*, *CCL2*, *CCL5*, *CCL17*, and *CCL22*) module scores for the colon and liver inflammatory and immunoregulatory TAMs. **C,** The bar plot shows the proportion (%) of each TAM cluster per cell-cycle phase (G1, S, and G2M) in the colon and liver. For the statistical analysis, the SEM was calculated according to the absolute cell count, and the unpaired nonparametric Mann–Whitney test was used to determine *P* values. **D,** The bar plot shows the module score of cell-cycle genes (*n* genes = 57) in the liver. For the statistical analysis, the SEM was calculated according to the absolute cell count, and the unpaired nonparametric Mann–Whitney test was used to determine *P* values. **E,** Double IHC for CD163/PCNA on liver metastases. In the peritumoral area of the liver, some cells are double positive for CD163 (red) and PCNA (brown). The nuclei are counterstained with hematoxylin. (*Continued on the following page.*)

comprising classic monocytes (cMono_CD14) characterized by high expression of *CD14* and the previously reported transcriptional features (43) mainly enriched in clusters *S100A8*_B0, *HLA-DRB1*_B1, *PPBP*_B2, *DPYD*_B3, and *ALAS2*_B4. On the other hand, *FCGR3A*_B5 comprised a minor population of nonclassic monocytes (ncMono_FCGR3A) showing high expression of *FCGR3A* and low levels of *CD14*. In addition to monocytes, we identified a small cluster of circulating pDCs enriched in the cluster *GZMB*_B6 (Supplementary Fig. S3A and S3B; Supplementary Table S1). Importantly and differently from healthy PBMCs (see "Materials and Methods" section, Supplementary Fig. S3C and S3D; refs. 26, 27), we did not find any monocytes showing cytotoxic transcriptional features, either among cMono_CD14 or in ncMono_FCGR3A (Supplementary Fig. S3B, S3D, and S3E). Of note, we found this signature only in TAMs from CRLM. Thus, we hypothesized a possible origin of these latter hepatic TAMs from circulating cytotoxic monocytes of patients with CRLM.

To provide a complete image of the three compartments and highlight tissue-specific heterogeneities, we integrated the three myeloid cell annotations from blood, primary colon cancer, and CRLM (Supplementary Fig. S4A). Correlation analysis identified the presence of shared transcriptional signatures of myeloid cells from matched samples of peripheral blood, colon, and liver of patients with CRLM (**Fig. 4A**). We observed significant high Pearson correlations between the inflammatory TAMs identified in liver cluster *S100A8*_L3 and those categorized as inflammatory TAMs within colon clusters *DOCK4*_C4 and *S100A9*_C6. These common traits between TAMs from different tumor compartments of patients with CRLM strongly suggest the presence of cells exerting similar functions. We also found high correlations between all liver and colon clusters in their high expression of HLA genes. Taken together, these results suggest interconnections between colon and liver TAMs that are mainly based on their functional characteristics (e.g., antigen-presentation, lipid-association, and angiogenesis). In addition, blood cluster *FCGR3A*_B5 and liver cluster *SMIM25*_L8 were transcriptionally similar, suggesting that nonclassic monocytes from peripheral blood may migrate to the liver and differentiate into inflammatory macrophages.

To identify the tissue-specific mechanisms regulating blood monocyte migration and their subsequent differentiation into macrophages within tissues, we then tracked their shifts by computing pseudotime trajectories. DCs were excluded from these analyses. We found that the trajectory split with the generation of three paths: path 0, path 1, and path 2 (**Fig. 4B** and **C**; Supplementary Fig. S4B). Blood cells were located on a single distinct branch (99.8%, path 0), consistent with their immature and undifferentiated status. Most colon macrophages localized on path 1 (92.6%), thus revealing the existence of a specific colon-associated path. The liver macrophages, on the other hand, localized in both paths 1 (34%) and 2 (59%), rather than a single branch, suggesting that liver macrophages can follow distinct differentiation programs. On path 2, the liver inflammatory TAM *S100A8*_L3 and *SMIM25*_L8 clusters mainly overlap with colon macrophages (Supplementary Fig. S4B). In contrast, liver-specific cytotoxic TAMs (*IL7R*_L0 and *CCL5*_L4) localized on the liver-specific path 2, endowed with high pseudotime values as they were characterized by a highly differentiated and matured phenotype. In addition, 7% of liver TAM cells colocalized onto the blood-enriched path 0. Therefore, to determine which cluster or group of clusters exhibited stronger blood-derivation features, we stratified and analyzed the amplitude of the pseudotime (**Fig. 4D**). This analysis confirmed that liver macrophages were more likely to originate from the bloodstream rather than the colon macrophages, and this was more evident in clusters *SMIM25*_L8, *APOC1*_L6, and *CCL4L2*_L5.

Liver immunoregulatory TAMs with large macrophage transcriptional profile show proliferative features

Lastly, we focused on examining the differences in the transcriptome and functional traits between the inflammatory and immunoregulatory TAMs in the colon and liver. DEG analysis between the colon and liver (Supplementary Fig. S5A; Supplementary Table S3) showed that TAMs in the colon were more inflammatory, with high levels of cytokine-associated genes (i.e., *CCL3L1*, *CXCL8*, *CCL20*, *CCL4L2*, *IL1B*, and *IL4L1*). In contrast, liver TAMs were characterized by an immune-regulatory signature with active metabolism, as indicated by ribosomal genes (i.e., *RPL11*, *RPL10*, and *RPL5*). The Reactome pathway–based analysis confirmed a higher transcriptional activation of inflammatory TAMs in the colon and of immunoregulatory TAMs in the liver (**Fig. 5A**). Colon TAMs rather than liver TAMs were highly associated with pathways involved in inflammatory cytokines production (e.g., IL1, IL6, IL12, and IL17). When looking at the metabolic pathways, liver TAMs were associated with protein synthesis, post-translational modifications, and proliferative features, which were not found to be associated with colon TAMs. Additionally, liver TAMs were more prone to exhibit immunosuppressive activity (**Fig. 5B**). These important differences between colon and liver TAMs highlight the pivotal role of tissue-specific macrophage phenotypes in shaping the local tumor milieu and the immunologic one, thus likely explaining the different clinical progression of cancer in these two different tissue compartments.

To investigate the proliferative properties observed in liver immunoregulatory TAMs, we analyzed the cell-cycle phases (G1, S, and G2M; **Fig. 5C**). By stratifying the colon and liver macrophage cell clusters across those three phases, we demonstrated that 100% of colon TAMs were comprised within the growth phase (G1 phase), whereas liver TAMs included cell clusters in G1, S, and G2M phases. In addition, to determine whether these proliferative features preferentially belonged to inflammatory or immunoregulatory TAMs in patients with CRLM, we computed a score of genes related to the cell-cycle proliferation phase (Supplementary Table S4), which in fact was found to be significantly higher in the immunoregulatory liver TAMs compared with inflammatory TAMs (**Fig. 5D**). We also

(*Continued*.) **F,** The Kaplan–Meier survival curve shows the proportion of disease-free survival in relation to the $CD163^{+}PCNA^{+}$ macrophage frequency in 18 CRLM specimens. Log-rank Mantel–Cox test used to determine *P* values. **G,** The PCA plots show the distribution of the liver macrophage clusters (L0–8) across the first three dimensions (PC1–3) based on their similarity according to the large TAM signature (top) or to the small TAM signature (bottom). The red arrows delineate the principal component 1 (PC1) dimension, which captures the highest variance and has been selected for downstream analysis. Dotted circles denote clusters characterized by high PC1 values. **H,** The box plot shows the distribution of the S and G2M phase gene scores (*n* genes = 20) computed in the most representative clusters enriched in the small (L3 and L8) and large (L2, L5, and L7) TAM scores, in which the inner line represents the median value. For the statistical analysis, the unpaired nonparametric Mann–Whitney test was used to determine *P* values. *, $P < 0.05$; **, $P < 0.01$; ***, $P < 0.001$; ****, $P < 0.0001$. CI, confidence interval; TCA, tricarboxylic acid.

identified a unique hallmark gene signature of these proliferating macrophages within S and G2M cell-cycle phases (Supplementary Fig. S5B).

By double IHC staining, we confirmed the presence of $CD163^+$ macrophages expressing PCNA at the invasive margins of CRLM (**Fig. 5E**). By plotting these data on a survival plot, we found a statistically significant difference between $CD163^+PCNA^{low}$ and $CD163^+PCNA^{high}$ patients: the 5-year disease-free survival went from 75% of the first group to 0% of the second group denoting more than sixfold risk of disease recurrence in case of $CD163^+$-$PCNA^{high}$ ($HR = 6.48$; 95% CI = 1.37–30.5; $P = 0.018$; **Fig. 5F**). These findings are consistent with the transcriptional data and, all together, they support the hypothesis that liver immunoregulatory and proliferative TAMs are associated with a negative prognosis.

Following our previous observation of morphologic differences among TAMs in patients with CRLM (13), we proceeded to assess whether the transcriptional classification of liver macrophage clusters herein reported (L0–8; **Fig. 3A**, **B**, and **D**) was associated with morphologic hallmarks that might lead to their identification on standard histologic slides. To this end, we drew upon insights from the bulk RNA-seq study on large and small TAMs to translate their transcriptomic profile into the scRNA-seq data (13). Based on the two signatures, we computed two independent gene-set scores derived using a principal component analysis (PCA), in which the principal component 1 (PC1) was used to capture the highest variation in gene-set expression across the liver macrophages as a continuous variable (see "Materials and Methods" section; **Fig. 5G**). The results showed that *S100A8*_L3 and *SMIM25*_L8 clusters were strongly enriched in the small-TAM score, whereas *HSPA6*_L2, *CCL4L2*_L5, and *SPATS2L*_L7 clusters defined large TAMs (**Fig. 5G**; Supplementary Fig. S5C). In addition, by analyzing the proliferation signature that characterized the liver TAMs in S and in G2M phases (Supplementary Fig. S5B), we observed that only large TAMs were enriched of that proliferation signature, indicating once again a relation between cell morphology, cell function, cell activity, and patients' prognosis (**Fig. 5H**).

Discussion

The present study characterizes the transcriptional heterogeneity of TAMs within the TMEs of matched human colorectal cancer and CRLM peritumoral specimens in patients with synchronous CRLM undergoing surgical resection of both primary tumor and liver metastasis.

The peritumoral area represents a highly dynamic zone in which tumor cells and immune components interact and mutually influence each other (13, 14, 47, 48). Within this microenvironment, tumor-educated immune cells can acquire immunosuppressive and protumorigenic features, ultimately dampening antitumor responses and promoting tumor progression. Spatial transcriptomic and histopathologic studies have further demonstrated that the peritumoral tissue, typically defined as the area within 100 μm from the liver parenchyma to the first row of tumor cells, harbors distinct prognostic and therapeutic significance in colorectal cancer and CRLM (49–51). The density and localization of tumor-infiltrating lymphocytes within this zone, as quantified by the Immunoscore, strongly correlate with clinical outcomes (52–55).

Among the immune populations shaping the TME, TAMs have emerged as key players, often described as double-edged because of their dual roles in cancer progression (38, 56, 57). In the context of CRLM, high frequencies of immunoregulatory TAMs are associated with poor prognosis and resistance to conventional therapies (14, 38). We previously reported that high frequencies of the so-called "large" TAMs exhibiting unique morphologic and transcriptomic features within the peritumoral area of CRLM correlate with worse prognosis (13, 14). These findings emphasize the critical role of TAMs in the progression and therapeutic resistance of CRLM, thus underscoring the need for targeted strategies to modulate their activity within the TME. However, the heterogeneity and different physiopathology of TAMs within the TMEs of matched colorectal cancer and CRLM had never been investigated in the context of the remarkable different clinical progressions of the same cancer. Similarly, the ontogeny of hepatic and gastrointestinal TAMs from circulating monocytes in a matched setting had never been explored.

Our scRNA-seq experiments first showed that inflammatory and immunoregulatory TAM clusters were present in both primary colorectal cancer and CRLM, thus confirming the complex immunologic heterogeneity of macrophages in cancer (33, 34). However, our trajectory analyses clearly showed that frequencies, transcriptome signatures, and functional relevance of these two dichotomic TAM families were remarkably different within the TMEs of the colon and liver, although both tissues are targeted by the same cancer. We found an inverse ratio between inflammatory and immunoregulatory TAMs within colon and liver TMEs, with great predominance of inflammatory TAM clusters in the colon and their immunoregulatory counterparts in the liver. Inflammation plays a dual role in the colorectal cancer immune escape, ultimately leading to liver metastasis (58). On one hand, it can enhance antitumor immunity by activating cytotoxic T cells and NK cells; on the other hand, chronic inflammation can support tumor progression by creating a protumorigenic microenvironment. Indeed, if an acute inflammatory response is not properly resolved, it can evolve into a chronic process inducing the activation of immunosuppressive macrophages, myeloid-derived suppressor cells and regulatory T cells (8, 59, 60). Additionally, the persistent inflammatory milieu also stimulates angiogenesis and extracellular matrix remodeling, thus further supporting tumor progression and metastatization (61). The preferential enrichment of inflammatory TAMs in the TME of primary colorectal cancer plays a paradoxical role, initially aiding in tumor control but ultimately enabling tumor evasion toward liver metastases (62), particularly in the early phases of the disease. We also reported here that these inflammatory colon-specific TAMs express high levels of inhibitory immune checkpoints ligands (e.g., PD-L1 and NECTIN2). This phenomenon represents a key pathogenic mechanism explaining colorectal cancer escape from immune surveillance (40).

In contrast, we found that the TME of CRLM was characterized by high frequencies of immunoregulatory TAMs, which greatly contribute to the establishment of immunosuppression, further enhanced by the high expression levels of several inhibitory checkpoints such as CTLA-4 and TIM-3. CTLA-4 promotes tumor escape by hampering the downstream signaling of costimulatory pathways through the internalization of CD80/CD86, which are critical for T-cell activation (41, 42). Additionally, we identified two pathologic liver-restricted clusters of $IL7R^{pos}$ cytotoxic macrophages characterized by an NK-like signature (e.g., *NKG7*, *GNLY*, *GZMA*, and *CTSW*), suggesting either the presence of TAM-mediated cytotoxicity against transformed cells or a TAM-mediated tumor immune-escape mechanism. Nevertheless, the origin of this atypical TAM population remains unclear. Two nonmutually exclusive hypotheses can be proposed. First, they may derive from cytotoxic monocytes that migrate and differentiate into macrophages;

alternatively, their cytotoxic gene signature could result from trogocytosis, a process whereby macrophages acquire membrane patches and cytotoxic molecules from other immune cells, such as NK cells or T cells, through partial phagocytosis (63–65). This latter phenomenon could explain the acquisition of NK-like features by liver TAMs within the metastatic niche. Further investigations are required to elucidate the precise mechanisms underlying the emergence of these cytotoxic TAMs in CRLM. Notably, our pseudotime analysis suggests that these cytotoxic TAMs likely originate from circulating monocytes that migrate and differentiate into macrophages preferentially in the liver rather than in the colon. Indeed, the *IL7R*^{pos} cytotoxic monocytes were first described under homeostatic physiologic conditions (43, 66). We report here that these two clusters of cytotoxic cells were completely absent in the bloodstream of patients with CRLM, whereas TAMs exhibiting a similar transcriptional profile were detected in the liver TME but were absent from both the colorectal cancer TME and healthy liver. Nonetheless, these clusters expressed inhibitory checkpoints (e.g., *TIGIT*, *LAG3*, and *CD96*), thus suggesting a suppression of their cytotoxic functions. Indeed, it has already been reported that TIGIT on macrophages can interact with its ligand CD155 leading to the inhibition of macrophage activation and promotion of an immunosuppressive environment that, in turn, hampers the production of proinflammatory cytokines (44, 67–69). Similarly, high expression of LAG3 has been reported to be coexpressed with CD68 on TAMs within an immunosuppressive TME (70–72). We also identified, exclusively in the hepatic TME of CRLM and not in primary colorectal cancer, the presence of unique immunoregulatory TAMs endowed with proliferative features. Proliferating TAMs showed the transcriptional characteristics of large TAMs, which were previously reported by us as those TAMs associated with worse prognosis (13). In this study, the finding of unique proliferation features of liver large TAMs clearly indicates a relation between cell morphology, cell function, cell activity and patients' prognosis that deserves to be ascertained.

The preferential enrichment of inflammatory TAMs in primary colorectal cancer and their immunoregulatory counterparts in the liver metastatic niche of CRLM in early stages of the disease mirrored the different clinical outcomes of the same cancer in these two tissues. This divergence aligns with clinical observations, as recurrence typically occurs in the liver, marked by the emergence of new CRLM lesions, even in absence of the primary colorectal cancer. Based on our data, the disease-free survival is clearly affected by the TAMs type in the context of CRLM. In other words, the development of new CRLMs during the course of the disease may be explained by the preferential enrichment of immuno-regulatory, proliferative, large TAMs in the CRLM TME, therefore representing a strong prognostic marker.

Overall, this study provides insights into the pathophysiology of early phases of synchronous CRLM in regard to tissue-specific TAM heterogeneity within the TME of the colon and liver. Although these results need to be confirmed on larger longitudinal cohorts of patients with CRLM, the remarkable imbalance between colon and liver macrophages together with the identification of liver-restricted proliferative and immunoregulatory large TAMs in CRLM help us to understand the early dynamic of primary colorectal cancer progression. Notably, it has been reported that macrophage phenotype and polarization can be reversed from an immune-suppressive state to a proinflammatory phenotype both *in vitro* and *in vivo* (73, 74). Thus, reprogramming the immune system to an antitumor state by blocking the transition of macrophages to an immunosuppressive phenotype, either alone or in combination with chemotherapy, may significantly enhance the antitumor response by reversing the immunosuppressive environment. This dual approach holds potential for improving the treatment outcomes for patients with CRLM (75).

Data Availability

The raw and processed scRNA-seq gene expression data generated in this study are publicly available in Gene Expression Omnibus using accession number of GSE298084. All the codes used for data processing and analysis are available in a public GitHub repository (https://github.com/pmarzano97/Synchro_CRLM.git). All other data generated in this study are available in the article and its supplementary files or from the corresponding author upon reasonable request.

Authors' Disclosures

F. Milana reports grants from the Ministry of Health during the conduct of the study. No disclosures were reported by the other authors.

Authors' Contributions

P. Marzano: Conceptualization, writing–original draft, writing–review and editing. **C. Soldani:** Conceptualization, writing–original draft, validation. **V. Cazzetta:** Methodology. **B. Franceschini:** Validation, methodology. **S. Terzoli:** Methodology. **A. Carletti:** Methodology. **M.A. Polidoro:** Methodology. **F. Marchesi:** Supervision. **M. Locati:** Supervision. **G. Basso:** Methodology. **A. Lleo:** Supervision. **G. Costa:** Methodology. **G. Torzilli:** Methodology. **F. Milana:** Methodology. **R. Piazza:** Supervision. **P. Spaggiari:** Methodology. **L. Di Tommaso:** Methodology. **J. Mikulak:** Conceptualization, supervision, writing–original draft. **D. Mavilio:** Conceptualization, supervision, writing–original draft, project administration, writing-review and editing. **M. Donadon:** Conceptualization, supervision, writing–original draft, project administration, writing–review and editing.

Acknowledgments

We thank all the patients who participated in this study. We would also like to thank the INDACO team for assistance in the use of computational resources of the high-performance computing facility at the University of Milano (http://www.indaco.unimi.it). This work was supported by 'Bando Ricerca Finalizzata 2018 of the Italian Ministry of Health' (ID = RF2018-12367150; principal investigator, M. Donadon). The funding agency had no role in the design of the study or collection and analysis of the data. The publication fee for this work was covered by the Italian Ministry of Health's "Ricerca Corrente" funding to the IRCCS Humanitas Research Hospital. P. Marzano is recipient of competitive fellowship awarded from the Ph.D. program of Experimental Medicine at the University of Milan.

Note

Supplementary data for this article are available at Cancer Immunology Research Online (http://cancerimmunolres.aacrjournals.org/).

Received January 10, 2025; revised May 14, 2025; accepted August 14, 2025; posted first August 19, 2025.

References

1. Sung H, Ferlay J, Siegel RL, Laversanne M, Soerjomataram I, Jemal A, et al. Global cancer statistics 2020: GLOBOCAN estimates of incidence and mortality worldwide for 36 cancers in 185 countries. CA Cancer J Clin 2021;71:209–49.
2. Hackl C, Neumann P, Gerken M, Loss M, Klinkhammer-Schalke M, Schlitt HJ. Treatment of colorectal liver metastases in Germany: a ten-year population-based analysis of 5772 cases of primary colorectal adenocarcinoma. BMC Cancer 2014;14:810.

3. Manfredi S, Lepage Cm, Hatem C, Coatmeur O, Faivre J, Bouvier A-M. Epidemiology and management of liver metastases from colorectal cancer. Ann Surg 2006;244:254–9.
4. Cucchetti A, Ferrero A, Cescon M, Donadon M, Russolillo N, Ercolani G, et al. Cure model survival analysis after hepatic resection for colorectal liver metastases. Ann Surg Oncol 2015;22:1908–14.
5. Siriwardena AK, Serrablo A, Fretland ÅA, Wigmore SJ, Ramia-Angel JM, Malik HZ, et al. Multisocietal European consensus on the terminology, diagnosis, and management of patients with synchronous colorectal cancer and liver metastases: an E-AHPBA consensus in partnership with ESSO, ESCP, ESGAR, and CIRSE. Br J Surg 2023;110:1161–70.
6. Halama N, Michel S, Kloor M, Zoernig I, Benner A, Spille A, et al. Localization and density of immune cells in the invasive margin of human colorectal cancer liver metastases are prognostic for response to chemotherapy. Cancer Res 2011;71:5670–7.
7. Mlecnik B, Van den Eynde M, Bindea G, Church SE, Vasaturo A, Fredriksen T, et al. Comprehensive intrametastatic immune quantification and major impact of Immunoscore on survival. J Natl Cancer Inst 2018;110:97–108.
8. Mantovani A, Allavena P, Sica A, Balkwill F. Cancer-related inflammation. Nature 2008;454:436–44.
9. Pollard JW. Tumour-educated macrophages promote tumour progression and metastasis. Nat Rev Cancer 2004;4:71–8.
10. Mantovani A, Marchesi F, Di Mitri D, Garlanda C. Macrophage diversity in cancer dissemination and metastasis. Cell Mol Immunol 2024;21:1201–14.
11. Forssell J, Öberg Ak, Henriksson ML, Stenling R, Jung A, Palmqvist R. High macrophage infiltration along the tumor front correlates with improved survival in colon cancer. Clin Cancer Res 2007;13:1472–9.
12. Steidl C, Lee T, Shah SP, Farinha P, Han G, Nayar T, et al. Tumor-associated macrophages and survival in classic Hodgkin's lymphoma. N Engl J Med 2010;362:875–85.
13. Donadon M, Torzilli G, Cortese N, Soldani C, Di Tommaso L, Franceschini B, et al. Macrophage morphology correlates with single-cell diversity and prognosis in colorectal liver metastasis. J Exp Med 2020;217:e20191847.
14. Costa G, Sposito C, Soldani C, Polidoro MA, Franceschini B, Marchesi F, et al. Macrophage morphology and distribution are strong predictors of prognosis in resected colorectal liver metastases: results from an external retrospective observational study. Int J Surg 2023;109:1311–7.
15. Young PE, Womeldorph CM, Johnson EK, Maykel JA, Brucher B, Stojadinovic A, et al. Early detection of colorectal cancer recurrence in patients undergoing surgery with curative intent: current status and challenges. J Cancer 2014;5:262–71.
16. Tian Y, Wang Y, Wen N, Wang S, Li B, Liu G. Prognostic factors associated with early recurrence following liver resection for colorectal liver metastases: a systematic review and meta-analysis. BMC Cancer 2024;24:426.
17. Liu W, Liu JM, Wang K, Wang HW, Xing BC. Recurrent colorectal liver metastasis patients could benefit from repeat hepatic resection. BMC Surg 2021;21:327.
18. Bruni E, Cimino MM, Donadon M, Carriero R, Terzoli S, Piazza R, et al. Intrahepatic CD69^{+}Vδ1 T cells re-circulate in the blood of patients with metastatic colorectal cancer and limit tumor progression. J Immunother Cancer 2022;10:e004579.
19. Wolf FA, Angerer P, Theis FJ. SCANPY: large-scale single-cell gene expression data analysis. Genome Biol 2018;19:15.
20. Wolock SL, Lopez R, Klein AM. Scrublet: computational identification of cell Doublets in single-cell transcriptomic data. Cell Syst 2019;8:281–91.e9.
21. Virshup I, Rybakov S, Theis FJ, Angerer P, Wolf FA. anndata: access and store annotated data matrices. J Open Source Softw 2024;9:4371.
22. Gayoso A, Lopez R, Xing G, Boyeau P, Valiollah Pour Amiri V, Hong J, et al. A Python library for probabilistic analysis of single-cell omics data. Nat Biotechnol 2022;40:163–6.
23. Traag VA, Waltman L, van Eck NJ. From Louvain to Leiden: guaranteeing well-connected communities. Sci Rep 2019;9:5233.
24. Becht E, McInnes L, Healy J, Dutertre CA, Kwok IWH, Ng LG, et al. Dimensionality reduction for visualizing single-cell data using UMAP. Nat Biotechnol 2018;37:38–44.
25. Ramachandran P, Dobie R, Wilson-Kanamori JR, Dora EF, Henderson BEP, Luu NT, et al. Resolving the fibrotic niche of human liver cirrhosis at single-cell level. Nature 2019;575:512–8.
26. Marzano P, Balin S, Terzoli S, Della Bella S, Cazzetta V, Piazza R, et al. Transcriptomic profile of TNF^{high} MAIT cells is linked to B cell response following SARS-CoV-2 vaccination. Front Immunol 2023;14:1208662.
27. Terzoli S, Marzano P, Cazzetta V, Piazza R, Sandrock I, Ravens S, et al. Expansion of memory Vδ2 T cells following SARS-CoV-2 vaccination revealed by temporal single-cell transcriptomics. NPJ Vaccin 2024;9:63.
28. Hao Y, Hao S, Andersen-Nissen E, Mauck WM III, Zheng S, Butler A, et al. Integrated analysis of multimodal single-cell data. Cell 2021;184:3573–87.e29.
29. Pedregosa F, Varoquaux G, Gramfort A, Michel V, Thirion B, Grisel O, et al. Scikit-learn: machine learning in Python. J Machine Learn Res 2011;12:2825–30.
30. Satija R, Farrell JA, Gennert D, Schier AF, Regev A. Spatial reconstruction of single-cell gene expression data. Nat Biotechnol 2015;33:495–502.
31. Trapnell C, Cacchiarelli D, Grimsby J, Pokharel P, Li S, Morse M, et al. The dynamics and regulators of cell fate decisions are revealed by pseudotemporal ordering of single cells. Nat Biotechnol 2014;32:381–6.
32. Beyer M, Mallmann MR, Xue J, Staratschek-Jox A, Vorholt D, Krebs W, et al. High-resolution transcriptome of human macrophages. PLoS One 2012;7:e45466.
33. Andrews TS, Atif J, Liu JC, Perciani CT, Ma XZ, Thoeni C, et al. Single-cell, single-nucleus, and spatial RNA sequencing of the human liver identifies cholangiocyte and mesenchymal heterogeneity. Hepatol Commun 2021;6:821–40.
34. Guilliams M, Scott CL. Liver macrophages in health and disease. Immunity 2022;55:1515–29.
35. Carenza C, Franzese S, Castagna A, Terzoli S, Simonelli M, Persico P, et al. Perioperative corticosteroid treatment impairs tumor-infiltrating dendritic cells in patients with newly diagnosed adult-type diffuse gliomas. Front Immunol 2022;13:1074762.
36. Xia P, Ji X, Yan L, Lian S, Chen Z, Luo Y. Roles of S100A8, S100A9 and S100A12 in infection, inflammation and immunity. Immunology 2024;171:365–76.
37. Lim SY, Yuzhalin AE, Gordon-Weeks AN, Muschel RJ. Tumor-infiltrating monocytes/macrophages promote tumor invasion and migration by upregulating S100A8 and S100A9 expression in cancer cells. Oncogene 2016;35:5735–45.
38. Mantovani A, Marchesi F, Malesci A, Laghi L, Allavena P. Tumour-associated macrophages as treatment targets in oncology. Nat Rev Clin Oncol 2017;14:399–416.
39. Ma RY, Black A, Qian BZ. Macrophage diversity in cancer revisited in the era of single-cell omics. Trends Immunol 2022;43:546–63.
40. Noy R, Pollard JW. Tumor-associated macrophages: from mechanisms to therapy. Immunity 2014;41:49–61.
41. Oyewole-Said D, Konduri V, Vazquez-Perez J, Weldon SA, Levitt JM, Decker WK. Beyond T-cells: functional characterization of CTLA-4 expression in immune and non-immune cell types. Front Immunol 2020;11:608024.
42. Smithy JW, Luke JJ. CD16+ macrophages: an emerging biomarker for combined CTLA-4 and PD-1 blockade. Clin Cancer Res 2023;29:2345–7.
43. Rigamonti A, Castagna A, Viatore M, Colombo FS, Terzoli S, Peano C, et al. Distinct responses of newly identified monocyte subsets to advanced gastrointestinal cancer and COVID-19. Front Immunol 2022;13:967737.
44. Zhang P, Liu X, Gu Z, Jiang Z, Zhao S, Song Y, et al. Targeting TIGIT for cancer immunotherapy: recent advances and future directions. Biomark Res 2024;12:7.
45. Brauneck F, Oliveira-Ferrer L, Muschhammer J, Sturmheit T, Ackermann C, Haag F, et al. Immunosuppressive M2 TAMs represent a promising target population to enhance phagocytosis of ovarian cancer cells in vitro. Front Immunol 2023;14:1250258.
46. Gigliotti CL, Dianzani C, Stoppa I, Monge C, Sutti S, Sblattero D, et al. Differential modulation of human M1 and M2 macrophage activity by ICOS-mediated ICOSL triggering. Int J Mol Sci 2023;24:2953.
47. Polidoro MA, Mikulak J, Cazzetta V, Lleo A, Mavilio D, Torzilli G, et al. Tumor microenvironment in primary liver tumors: a challenging role of natural killer cells. World J Gastroenterol 2020;26:4900–18.
48. Soldani C, De Simone G, Polidoro MA, Morabito A, Franceschini B, Colombo FS, et al. Riboflavin-LSD1 axis participates in the in vivo tumor-associated macrophage morphology in human colorectal liver metastases. Cancer Immunol Immunother 2024;73:63.
49. Giuliante F, Viganò L, De Rose AM, Mirza DF, Lapointe R, Kaiser G, et al. Liver-first approach for synchronous colorectal metastases: analysis of 7360 patients from the LiverMetSurvey registry. Ann Surg Oncol 2021;28:8198–208.
50. Garcia-Vicién G, Mezheyeuski A, Micke P, Ruiz N, Ruffinelli JC, Mils K, et al. Spatial Immunology in liver metastases from colorectal carcinoma according to the histologic growth pattern. Cancers (Basel) 2022;14:689.

51. Wood CS, Pennel KAF, Leslie H, Legrini A, Cameron AJ, Melissourgou-Syka L, et al. Spatially resolved transcriptomics deconvolutes prognostic histological subgroups in patients with colorectal cancer and synchronous liver metastases. Cancer Res 2023;83:1329–44.
52. Williams DS, Mouradov D, Jorissen RN, Newman MR, Amini E, Nickless DK, et al. Lymphocytic response to tumour and deficient DNA mismatch repair identify subtypes of stage II/III colorectal cancer associated with patient outcomes. Gut 2019;68:465–74.
53. Lee H, Sha D, Foster NR, Shi Q, Alberts SR, Smyrk TC, et al. Analysis of tumor microenvironmental features to refine prognosis by T, N risk group in patients with stage III colon cancer (NCCTG N0147) (Alliance). Ann Oncol 2020;31:487–94.
54. Pagès F, Mlecnik B, Marliot F, Bindea G, Ou FS, Bifulco C, et al. International validation of the consensus immunoscore for the classification of colon cancer: a prognostic and accuracy study. Lancet 2018;391:2128–39.
55. Mlecnik B, Bindea G, Angell HK, Maby P, Angelova M, Tougeron D, et al. Integrative analyses of colorectal cancer show Immunoscore is a stronger predictor of patient survival than microsatellite instability. Immunity 2016;44:698–711.
56. Cassetta L, Pollard JW. Targeting macrophages: therapeutic approaches in cancer. Nat Rev Drug Discov 2018;17:887–904.
57. Locati M, Curtale G, Mantovani A. Diversity, mechanisms, and significance of macrophage plasticity. Annu Rev Pathol 2020;15:123–47.
58. Burgos-Molina AM, Téllez Santana T, Redondo M, Bravo Romero MJ. The crucial role of inflammation and the immune system in colorectal cancer carcinogenesis: a comprehensive perspective. Int J Mol Sci 2024;25:6188.
59. Grivennikov SI, Karin M. Inflammation and oncogenesis: a vicious connection. Curr Opin Genet Dev 2010;20:65–71.
60. Zhao H, Wu L, Yan G, Chen Y, Zhou M, Wu Y, et al. Inflammation and tumor progression: signaling pathways and targeted intervention. Signal Transduct Target Ther 2021;6:263.
61. Grivennikov SI, Greten FR, Karin M. Immunity, inflammation, and cancer. Cell 2010;140:883–99.
62. Terzić J, Grivennikov S, Karin E, Karin M. Inflammation and colon cancer. Gastroenterology 2010;138:2101–14.e5.
63. Joly E, Hudrisier D. What is trogocytosis and what is its purpose? Nat Immunol 2003;4:815.
64. Almishri W, Swain LA, D'Mello C, Le TS, Urbanski SJ, Nguyen HH. ADAM metalloproteinase domain 17 regulates cholestasis-associated liver injury and sickness behavior development in mice. Front Immunol 2021;12:779119.
65. Miyake K, Karasuyama H. The role of trogocytosis in the modulation of immune cell functions. Cells 2021;10:1255.
66. Villani AC, Satija R, Reynolds G, Sarkizova S, Shekhar K, Fletcher J, et al. Single-cell RNA-seq reveals new types of human blood dendritic cells, monocytes, and progenitors. Science 2017;356:eaah4573.
67. Sathe A, Ayala C, Bai X, Grimes SM, Lee B, Kin C, et al. GITR and TIGIT immunotherapy provokes divergent multicellular responses in the tumor microenvironment of gastrointestinal cancers. Genome Med 2023;15:100.
68. Brauneck F, Fischer B, Witt M, Muschhammer J, Oelrich J, da Costa Avelar PH, et al. TIGIT blockade repolarizes AML-associated TIGIT(+) M2 macrophages to an M1 phenotype and increases CD47-mediated phagocytosis. J Immunother Cancer 2022;10:e004794.
69. Brauneck F, Fischer B, Wellbrock J, Bokemeyer C, Schulze zur Wiesch J, Haag F, et al. Blockade of tigit on AML-derived M2 macrophages results in reprograming into the M1 phenotype and enhances CD47-mediated phagocytosis. Blood 2021;138:3351.
70. Keane C, Law SC, Gould C, Birch S, Sabdia MB, Merida de Long L, et al. LAG3: a novel immune checkpoint expressed by multiple lymphocyte subsets in diffuse large B-cell lymphoma. Blood Adv 2020;4:1367–77.
71. Marcq E, Waele J, Audenaerde JV, Lion E, Santermans E, Hens N, et al. Abundant expression of TIM-3, LAG-3, PD-1 and PD-L1 as immunotherapy checkpoint targets in effusions of mesothelioma patients. Oncotarget 2017;8:89722–35.
72. Arimura K, Hiroshima K, Nagashima Y, Nakazawa T, Ogihara A, Orimo M, et al. LAG3 is an independent prognostic biomarker and potential target for immune checkpoint inhibitors in malignant pleural mesothelioma: a retrospective study. BMC Cancer 2023;23:1206.
73. Guiducci C, Vicari AP, Sangaletti S, Trinchieri G, Colombo MP. Redirecting in vivo elicited tumor infiltrating macrophages and dendritic cells towards tumor rejection. Cancer Res 2005;65:3437–46.
74. Saccani A, Schioppa T, Porta C, Biswas SK, Nebuloni M, Vago L, et al. p50 nuclear factor-kappaB overexpression in tumor-associated macrophages inhibits M1 inflammatory responses and antitumor resistance. Cancer Res 2006;66:11432–40.
75. Mills CD, Lenz LL, Harris RA. A breakthrough: macrophage-directed cancer immunotherapy. Cancer Res 2016;76:513–6.